Automated detection and temporal monitoring of crevasses using remote sensing and their implications for glacier dynamics

Anshuman BHARDWAJ,[1,2] Lydia SAM,[2,3] Shaktiman SINGH,[2] Rajesh KUMAR[2]

[1]*TERI University, New Delhi, India*
[2]*Sharda University, Greater Noida, India*
[3]*Defence Research & Development Organisation, New Delhi, India*
Correspondence: Anshuman Bhardwaj <anshuman.teri@gmail.com>

ABSTRACT. Detailed studies on temporal changes of crevasses and their linkage with glacier dynamics are scarce in the Himalayan context. Observations of temporally changing surficial crevasse patterns and their orientations are suggestive of the processes that determine seasonal glacier flow characteristics. In the present study, on a Himalayan valley glacier, changing crevasse patterns and orientations were detected and mapped on Landsat 8 images in an automated procedure using the ratio of Thermal Infrared Sensor (TIRS) band 10 to Optical Land Imager (OLI) shortwave infrared (SWIR) band 6. The ratio was capable of mapping even crevasses falling under mountain shadows. Differential GPS observations suggested an average error of 3.65% and root-mean-square error of 6.32 m in crevasse lengths. A year-round observation of these crevasses, coupled with field-based surface velocity measurements, provided some interesting interpretations of seasonal glacier dynamics.

KEYWORDS: crevasses, glacier mechanics, mountain glaciers, remote sensing

1. INTRODUCTION

Crevasses are frequently seen on the surfaces of alpine glaciers and polar ice sheets. Crevasses are fractures in glacier ice which are formed under stresses developed due to vertical variations of ice velocity (Paterson, 1994; Van der Veen, 1998). They are hazardous during field activities, particularly when buried under snow (Singh and others, 2013). The orientation of crevasses can be correlated with the surface strain rate and thus can be used to understand the ice dynamics (Holdsworth, 1969; Hambrey and Muller, 1978; Vornberger and Whillans; 1990; Harper and others, 1998). Based on the critical fracture strain, a classification of crevassing was first proposed by Hughes (1983), but this was not based on any directly measured parameter (Vaughan, 1993). Study of the changing orientation and pattern of crevasses can provide information about the direction of propagation of the principal stresses generated (Vornberger and Whillans, 1986). Temporal monitoring of the crevasse pattern is considered useful in studying glacier dynamics through measurements of glacier motion and deformation (Whillans and Tseng, 1995). The detection and mapping of existing as well as emerging crevasses are also very significant in terms of safety measures, particularly in polar research (Zhou and others, 2008). With advances in digital photogrammetry and availability of high-resolution satellite images since the early 1990s, many important studies related to the monitoring of movement of surface crevasses have contributed to glacier research (Bindschadler and Scambos, 1991; Whillans and others, 1993; Whillans and Tseng, 1995).

Remote sensing of surface crevasses is still in its early years as a topic of research. In most instances, ground-based ground-penetrating radar (GPR) has been utilized in polar regions for the detection of buried crevasses (Shabtaie and Bentley, 1987; Retzlaff and Bentley, 1993). In the past decade, there has been a surge in similar studies utilizing ground-based and airborne GPR in polar regions (Taurisano and others, 2006; Luckman and others, 2012; Lever and others, 2013). Zhou and others (2008) used both microwave and optical bands for crevasse detection. They concluded that because of their penetrative capabilities, microwaves could detect crevasses even under snow bridges. But as a result of directional complexities of the radar beam and crevasse orientation, there was a possibility of non-detection of some hidden crevasses. In continuation of that study, they further utilized optical data of SPOT (Satellite Pour l'Observation de la Terre) and ASTER (Advanced Space-borne Thermal Emission and Reflection Radiometer) to detect crevasses. They performed texture analysis using a Gabor wavelet filter to locate crevasses. A major weakness of their study was the absence of fieldwork to validate the results. The number of studies of crevasse detection on alpine glaciers is very limited (Zamora and others 2007; Eder and others, 2008). In a pioneering study in the case of the Indian Himalaya, Singh and others (2013) used GPR in both 250 MHz frequency ground mode and 350 MHz airborne mode. They validated the results obtained from airborne GPR by comparing them with the identified signatures of open and hidden crevasses in ground-based GPR profiles obtained at the same time.

We conducted a literature survey which suggested quite a few research gaps in the utilization of remote sensing for detection and mapping of crevasses. A very prominent research gap is the joint use of optical and thermal bands for this purpose. Most previous studies have utilized the microwave bands. In addition, most have focused exclusively on the large fractures present on polar ice sheets. The possible implications of crevasses on alpine glaciers for glacier dynamics have been little studied. Another limitation is the inadequate availability of free optical and thermal remote-sensing data for a wide user community. Any algorithm developed for freely available data such as Landsat images (which have both optical and thermal bands) will benefit a large number of researchers. As

https://doi.org/10.3189/2016AoG71A496 Published online by Cambridge University Press

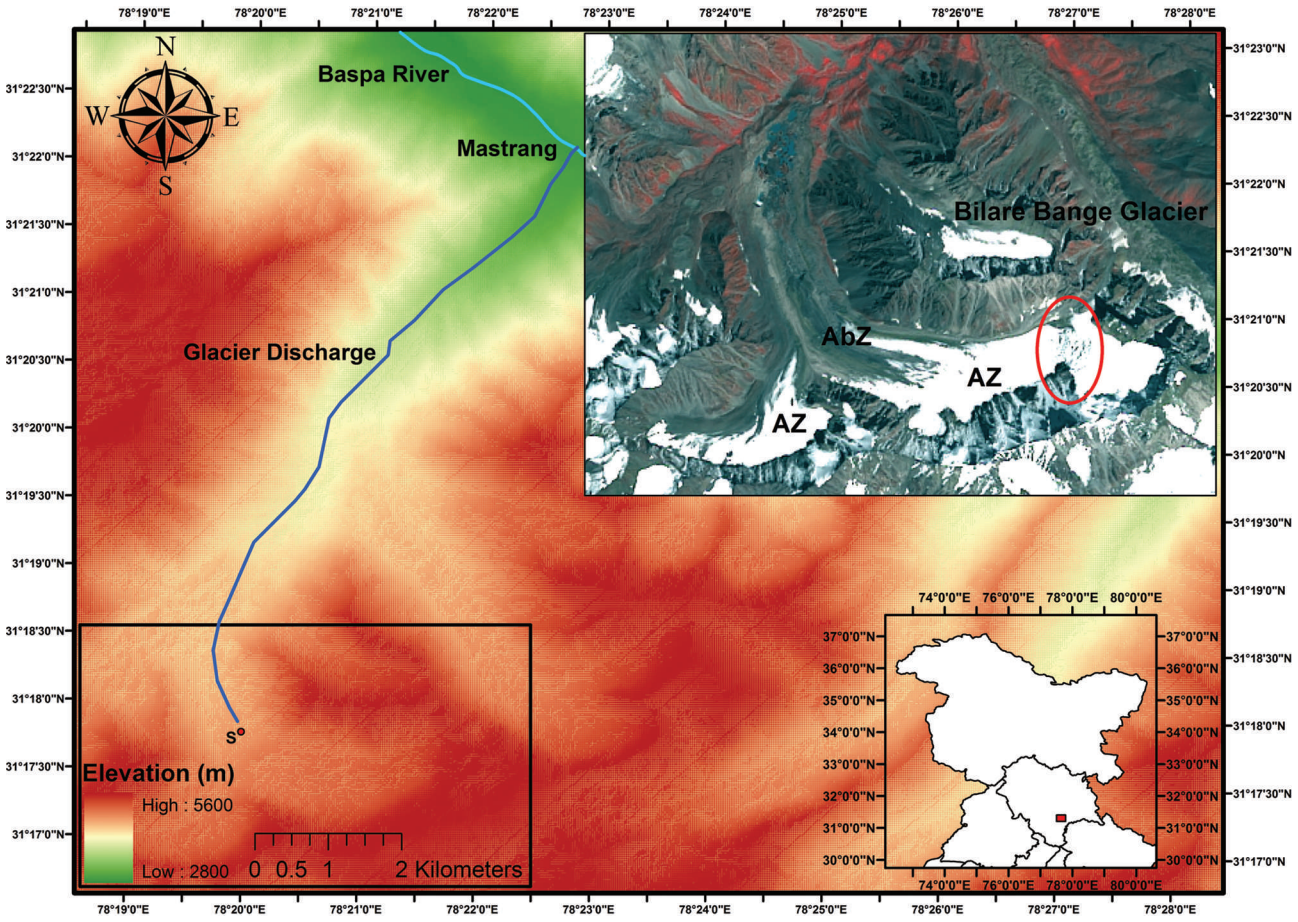

Fig. 1. Location map of the study area. The hillshade view is generated using ASTER GDEM V2 with corresponding elevation information. Upper right inset shows pan-sharpened Landsat 8 FCC (false-colour composite) (RGB-543) of 18 September 2013. AbZ: ablation zone; AZ: accumulation zone; red ellipse: icefall with many transverse crevasses.

another challenge, in the course of monitoring of a large glaciated area, there is a need to automate crevasse detection, in order to save time and effort. At optical wavelengths, shadows are always an obstacle to detection. The most important current research gap, in the case of optical remote-sensing-based crevasse mapping, is the lack of field validation on the dates of image acquisition. A successful automated algorithm is one which yields error estimates of orientation, length, geolocation, and additionally the possible reasons for those errors. Fieldwork can supply these estimates.

The present work is an attempt to address all the above-mentioned research gaps. In addition, it attempts to understand the implications of changing crevasse patterns and orientations for glacier dynamics by linking the results with field observations made during satellite pass. Bhardwaj and others (2015a), in a recent study, successfully detected surface crevasses on Himalayan glaciers, even under mountain shadow zones. They utilized Landsat 8 Operational Land Imager (OLI) and Thermal Infrared Sensor (TIRS) data for the detection. However, their study was essentially directed towards simultaneous mapping of various glacial facies and supraglacial debris. Therefore, their proposed automated algorithm is complex, involving several bands, and needs to be simplified and made specific for crevasse detection and mapping. The present study works towards simplification and specialization of the algorithm of Bhardwaj and others (2015a) for automated crevasse detection and mapping.

2. STUDY AREA AND DATA USED

2.1. Study area

The automated crevasse detection algorithm was developed and validated for Shaune Garang glacier, located in the Baspa river basin of Himachal Pradesh, India (31°16′–31°18′ N, 78°18′–78°22′ E; Fig. 1). The total area of this glacier is nearly 4 km^2. The main trunk is 4.5 km long and flows from east to west (Fig. 1). The snout was located at ~4500 m a.s.l. and was found during a field visit on 21 September 2014 to be ~1230 m above the present confluence of the Shaune Garang discharge stream and the Baspa river (Bhardwaj and others, 2015a). The glacier was selected for fieldwork because it had a relatively gentle average slope with fewer steep sections, favourable for easy and quick ascent along a transect on the day of satellite pass, and a very prominent icefall with many suitably large crevasses which were likely to be detectable in Landsat 8 imagery (Fig. 1).

2.2. Data used

Landsat 8 was launched by NASA on 11 February 2013 (Joshi and others, 2013). The spatial resolutions or grid sizes are different in the different bands (http://landsat.gsfc.nasa.gov). The OLI captures in the visible, NIR (near-infrared) and SWIR (shortwave infrared) regions with a spatial resolution of 30 m. The TIRS captures in the thermal infrared with a grid size of 100 m. There is an additional panchromatic band of 15 m spatial resolution spread across the visible

https://doi.org/10.3189/2016AoG71A496 Published online by Cambridge University Press

Table 1. Details of used Landsat 8 data (WRS path/row 146/038)

Dates:			
2013: 30 June, 18 September, 20 October, 5 November, 21 November, 23 December 2014: 14 April, 16 May, 17 June, 4 August, 20 August, 21 September, 23 October			
Bands used:			
Band	Name	Wavelength μm	Spatial resolution m
Operational Land Imager (OLI)			
6	Shortwave infrared	1.57–1.65	30
8	Panchromatic	0.50–0.68	15
Thermal Infrared Sensor (TIRS)			
10	Thermal band 1	10.60–11.19	100

wavelengths. As a spectral improvement, the OLI is equipped with two additional very narrow and specialized bands: band 1 (coastal/aerosol) and band 9 (cirrus cloud). The improvement in radiometric resolution of Landsat 8 bands (acquisition at 12 bits) is also a remarkable enhancement over traditional Landsat data (8 bits). The data and the bands used for the study are listed in Table 1.

In total, 15 bamboo stakes were installed on the glacier in September 2013 for differential GPS (DGPS) velocity measurements using Trimble R7/5700 dual frequency receivers (one base and two rovers). Three stakes in the icefall zone are used to discuss outcomes of the present study (Table 2). The horizontal precision 1σ (scaled) and the vertical precision 1σ (scaled) (https://www.fgdc.gov/standards/projects/FGDC-standards-projects/accuracy/part3/draft_chapter3), for each point, were <0.5 m. Solution types for all the points were fixed (Naesset, 2001) for zero-order polynomial correction to ensure high-precision DGPS positioning. The average RMSE (root-mean-square error) in measurements was reported to be ~0.05 m. All points were collected in dual frequency mode (L1/L2) using static mode or solution (corrections were applied in the laboratory) along with the zero-order polynomial (linear) correction method. The base station position was the same for all points. A total of 15 ground control points (GCPs) in stable areas outside the glacier were also acquired with the same precision. These GCPs were used for geo-rectification of the satellite scenes. An additional 34 DGPS observations were made on 18 September 2013 and 21 September 2014 for validating the automated detection algorithm by comparing the lengths of mapped crevasses with field observations. For validation, we have calculated crevasse lengths using only the coordinates of the two endpoints.

3. METHODOLOGY

The proposed automated methodology for detecting and characterizing surface crevasses is given in Figure 2. The steps are detailed in the subsections below.

3.1. Conversion of OLI and TIRS DN (digital number) to TOA (top-of-atmosphere) reflectance and at-satellite brightness temperature

The United States Geological Survey (USGS) official website gives the equations (https://landsat.usgs.gov/Landsat8_Using_Product.php) and recent calibration notices (https://landsat.usgs.gov/calibration_notices.php) for obtaining TOA reflectance (ρ_λ)

$$\rho_\lambda = \left(M_\rho Q_{\text{cal}} + A_\rho\right) / \sin\ \theta_{\text{SE}} \quad (1)$$

and at-satellite brightness temperature (T)

$$T = K_2 / \ln\left[1 + K_1/(M_L Q_{\text{cal}} + A_L - 0.29\ )\right] \quad (2)$$

where T is in kelvin, M_ρ and M_L are band-specific multiplicative rescaling factors, Q_{cal} are digital numbers (quantized and calibrated standard-product pixel values), A_ρ and A_L are band-specific additive rescaling factors, θ_{SE} is the sun elevation angle at the scene centre in degrees, K_1 and K_2 are band-specific thermal conversion constants and the value 0.29 refers to the TIRS thermal band 10 calibration constant (14 November 2013, calibration notice, http://landsat.usgs.gov/calibration_notices.php).

We did not correct for atmospheric effects on upwelling radiation received at satellite altitude. The reflectances of the land-cover features in the study area are sufficiently different that, especially with 12-bit radiometry, atmospheric effects are unlikely to affect their spectral separation (Lu and others, 2002). Since NASA is yet to release formal guidelines for the atmospheric correction of Landsat 8 bands, we chose not to use predefined algorithms derived from other datasets, which otherwise might have rendered pixel values (surface reflectance) drastically.

3.2. Pan-sharpening of OLI bands and resampling of at-satellite brightness temperature band 10

The TOA reflectance bands were pan-sharpened using ρ_λ band 8 (panchromatic) to improve their spatial resolution. Initially the proposed band ratios were calculated without pan-sharpening. Compared to the vast fractures on polar ice sheets, the crevasses on Himalayan glaciers are smaller in length and width. Therefore the automated mapping accuracy of these smaller alpine glacier crevasses significantly

Table 2. Details of DGPS points and on-field displacements. Latitudes and longitudes are in decimal degrees

Point ID	18 Sep 2013		20 Oct 2013		21 Sep 2014		23 Oct 2014		Displacement	
	Lat.	Long.	Lat.	Long.	Lat.	Long.	Lat.	Long.	Monthly (Sep–Oct 2013)	Monthly (Sep–Oct 2014)
	°	°	°	°	°	°	°	°	m	m
1	31.2930634	78.3564305	31.2930623	78.3564264	31.2930558	78.3563711	31.2930547	78.3563640	0.40	0.68
2	31.2917492	78.3565987	31.2917501	78.3565942	31.2917590	78.3565574	31.2917611	78.3565496	0.43	0.78
3	31.2903526	78.3564185	31.2903539	78.3564151	31.2903619	78.3563956	31.2903640	78.3563914	0.35	0.46

https://doi.org/10.3189/2016AoG71A496 Published online by Cambridge University Press

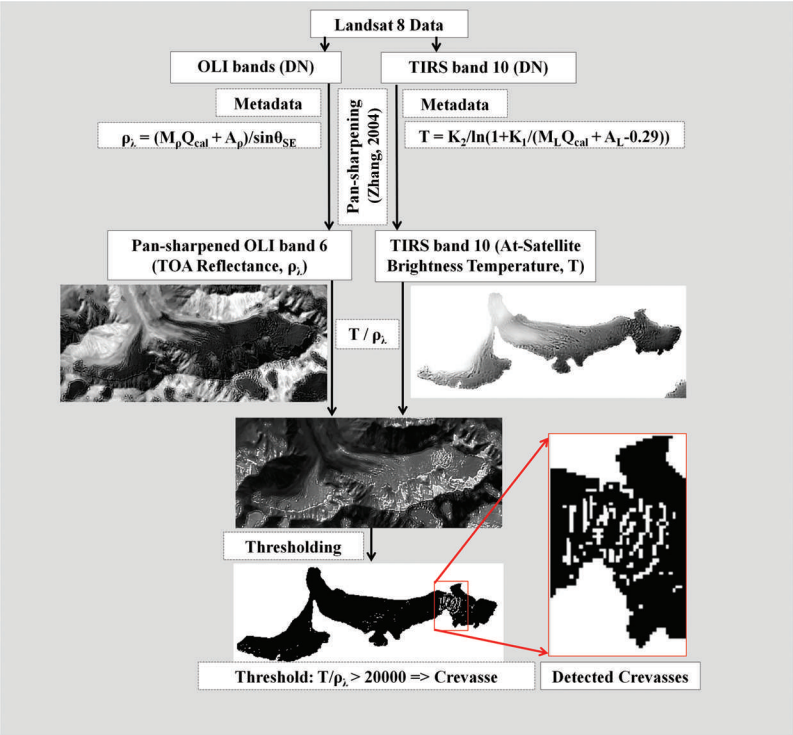

Fig. 2. Methodology adopted for automated detection and mapping of crevasses.

improved after pan-sharpening. Several existing methods of data fusion were attempted for pan-sharpening of OLI TOA reflectance bands. The pan-sharpening cannot add any new spectral information to an existing spatial field. Here we were simply concerned about preserving the information content of the lower-resolution bands while lowering their pixel dimensions.

The statistics-based fusion technique given by Zhang (2004) gave best results (Bhardwaj and others, 2015b); in addition to improvement in spatial resolution, this technique also preserved the spectral characteristics of the bands (Fig. 3). The at-satellite brightness temperature band 10 was resampled to 15 m grid size using bicubic interpolation (Rifman, 1973) for further band-ratioing.

3.3. Point-to-image co-registration

The acquired 15 GCPs were used for point-to-image co-registration of all the satellite scenes. The observed RMSE for

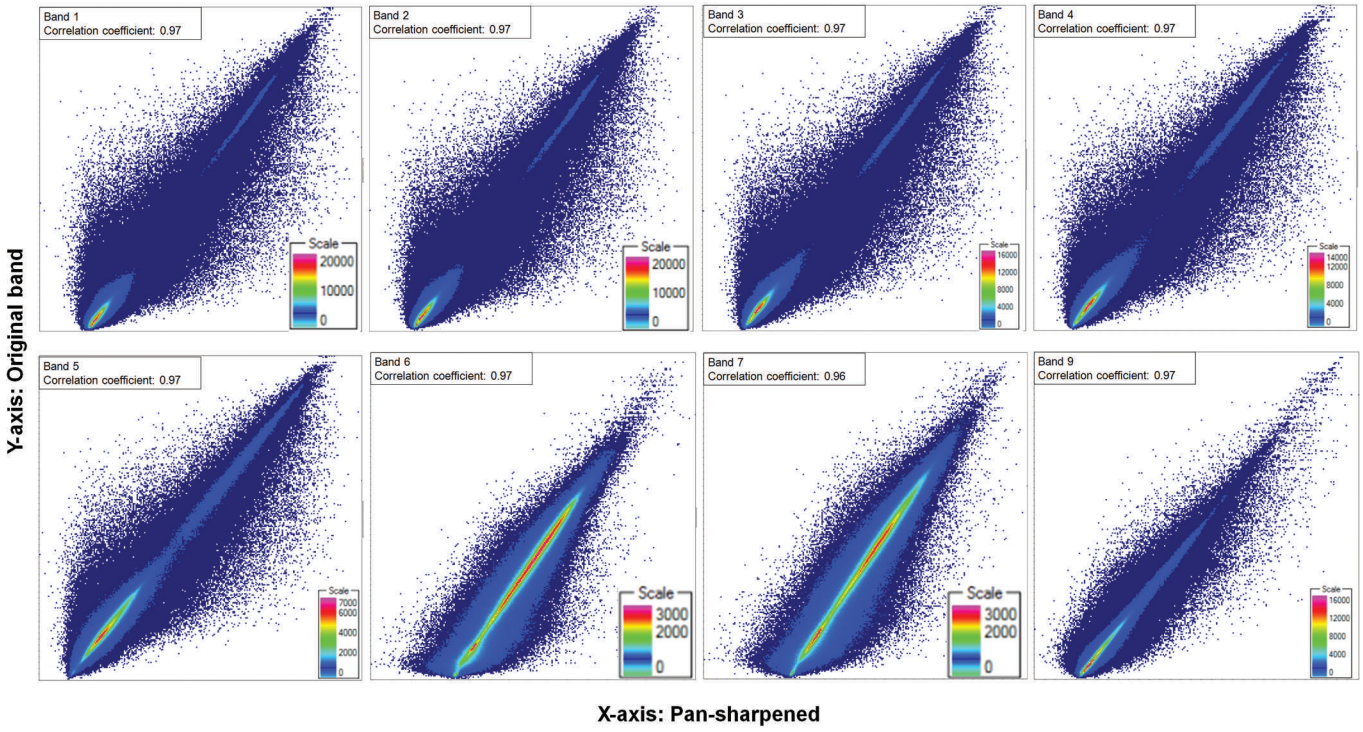

Fig. 3. Correlation analysis between original spectral OLI bands and pan-sharpened bands.

https://doi.org/10.3189/2016AoG71A496 Published online by Cambridge University Press

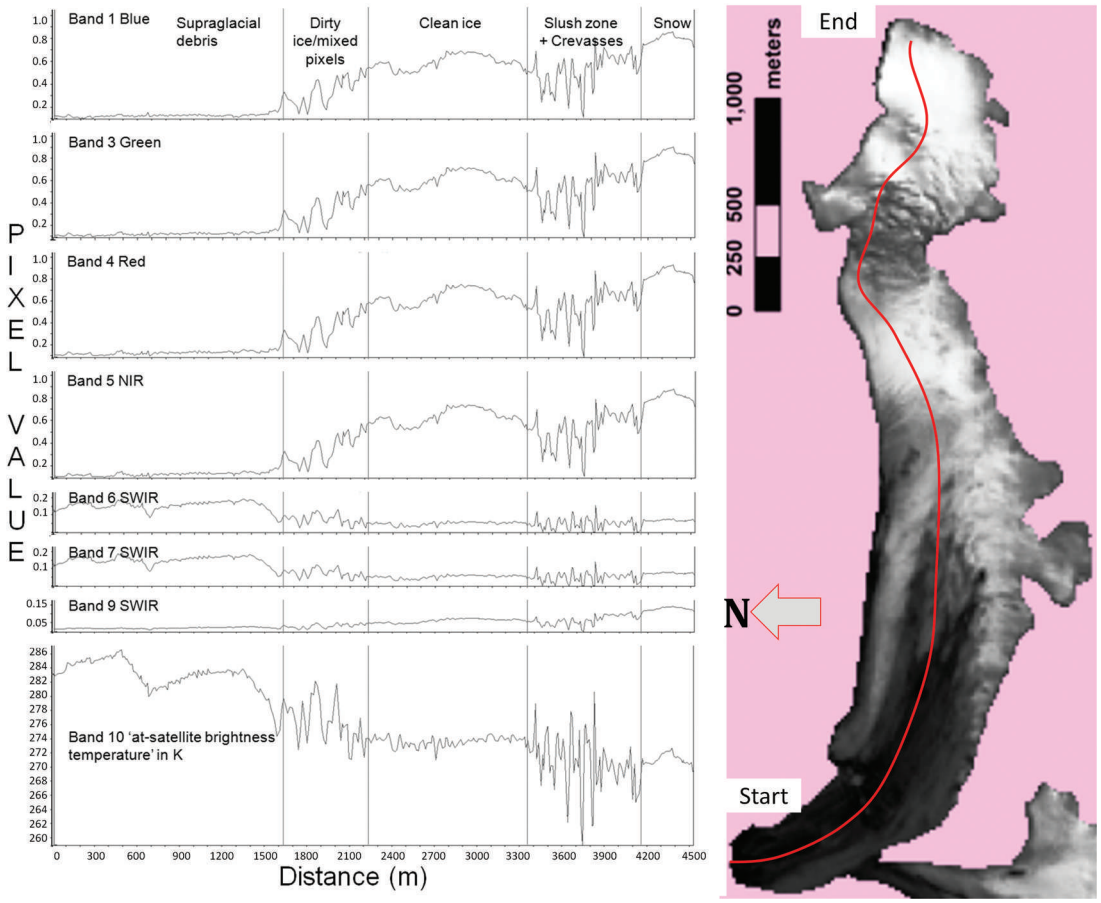

Fig. 4. Spectral profiles of TOA reflectance and brightness temperature of Landsat 8 bands of 18 September 2013 along the field transect observed on the same day.

all the scenes after co-registration was found to be in the range 0.12–0.15 (in pixel). This step was crucial for ensuring accurate correlation between the displacements measured in the field and the outcomes of the automated crevasse detection.

3.4. Selection of the appropriate bands, band-ratioing and thresholding

The transect along which the field observations were made at the time of satellite acquisition on 18 September 2013 is shown in Figure 4. The changes in the surface features along the transect were documented, which further helped in interpreting the spectral profiles also shown in Figure 4.

These spectral profiles show that visible and NIR bands capture more subtle variations in parts of the glacier other than supraglacial debris (ice and snow facies). By contrast, SWIR bands 6 and 7 show minor variations in the regions of supraglacial debris cover more prominently. Band 9 (SWIR) with very low reflectance values represents a smoother profile, i.e. it did not represent subtle surface variations. The spectral profile of at-satellite brightness temperature derived from thermal band 10 typically presents a clear distinction between different surface types in the slush zone, where there are many large crevasses. This brightness temperature band was considered appropriate as a base layer, and the contrast of the crevasse pixels with their surroundings was expected to be enhanced using reflectance properties of OLI bands. For selected OLI bands, Table 3 gives average reflectance values along the transect for various surface types.

As is clear from Table 3, band 6 has the lowest reflectance only for snow and ice. This means that the at-satellite brightness temperature, when divided by the TOA reflectance of different bands, will produce greater band ratios for snow/ice pixels when the band in the denominator is band 6. In the present study, the brightness temperature of the glacier surface varied within a range of 26 K with minimum values (from around 260 to 270 K) for crevasses and maximum values of ~286 K for supraglacial debris, with intermediate temperatures representing snow and ice. These values are likely to be similar for other glaciers. The reflectance values for band 6 were sufficiently low (with average ρ_λ of 0.055) for ice and snow to highlight the presence of fractures. The ratio was significantly higher for crevasses, and a threshold of $T_b/\rho_\lambda > 20\,000$ was found to be optimal for assigning pixels to crevasses.

Table 3. Average TOA reflectance values and standard deviations along the transect for different surface types in case of various OLI bands (Bhardwaj and others, 2015a)

Band	Snow	Ice	Supraglacial debris
1	0.91 ± 0.069	0.67 ± 0.051	0.14 ± 0.019
5	0.92 ± 0.072	0.71 ± 0.051	0.13 ± 0.020
6	0.06 ± 0.008	0.05 ± 0.051	0.15 ± 0.024
7	0.07 ± 0.009	0.05 ± 0.051	0.15 ± 0.023
9	0.15 ± 0.022	0.08 ± 0.051	0.02 ± 0.004

https://doi.org/10.3189/2016AoG71A496 Published online by Cambridge University Press

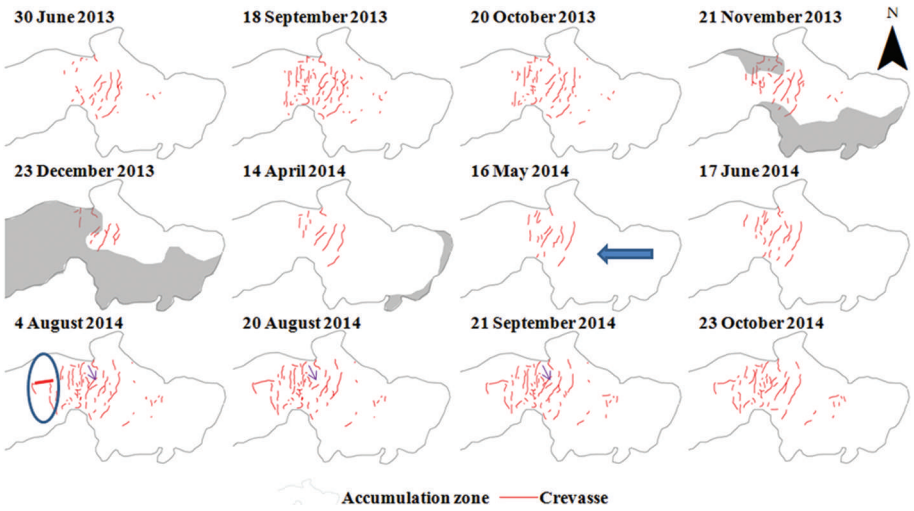

Fig. 5. Detected crevasses in the accumulation zone of the glacier. Blue ellipse marks the increasing number of newly developing crevasses towards the end of the ice facies and the start of the slush zone. Thickened red line within the blue ellipse shows the longitudinal crevasse of ~150 m length. The purple arrows show the crevasse which closed and reopened. The blue arrow shows the direction of the glacier flow. The grey shaded portion represents the area within mountain shadow in November, December and April.

4. RESULTS AND VALIDATION

The detected crevasses shown in the inset in Figure 2 are prominent at the transition of ice to snow facies, usually marked by the presence of a slush zone for Shaune Garang glacier during September (Bhardwaj and others, 2015a). The detected crevasses for this zone were vectorized for the months given in Table 1. The maps showing locations and patterns of these fractures are given in Figure 5. An interesting observation is illustrated by the blue ellipse in Figure 5, that suggests an increasing number of newly developing crevasses towards the end of the ice facies and the start of the slush zone.

Another observation, depicted by the red line within the blue ellipse in Figure 5 is the development of a longitudinal fracture of ~150 m length. The purple arrows in the same figure show a crevasse of ~183 m length which disappeared and reappeared within a time span of 47 days. This crevasse is situated in the icefall on a very steep slope (approximately 50–60°; Fig. 6).

The icefall experiences regular avalanching, which is one of the reasons for the frequent changes of crevasse pattern in this zone. In fact an avalanche was observed in the field during this period (4 August to 21 September) and the field photographs of the crevasse are shown in Figure 7.

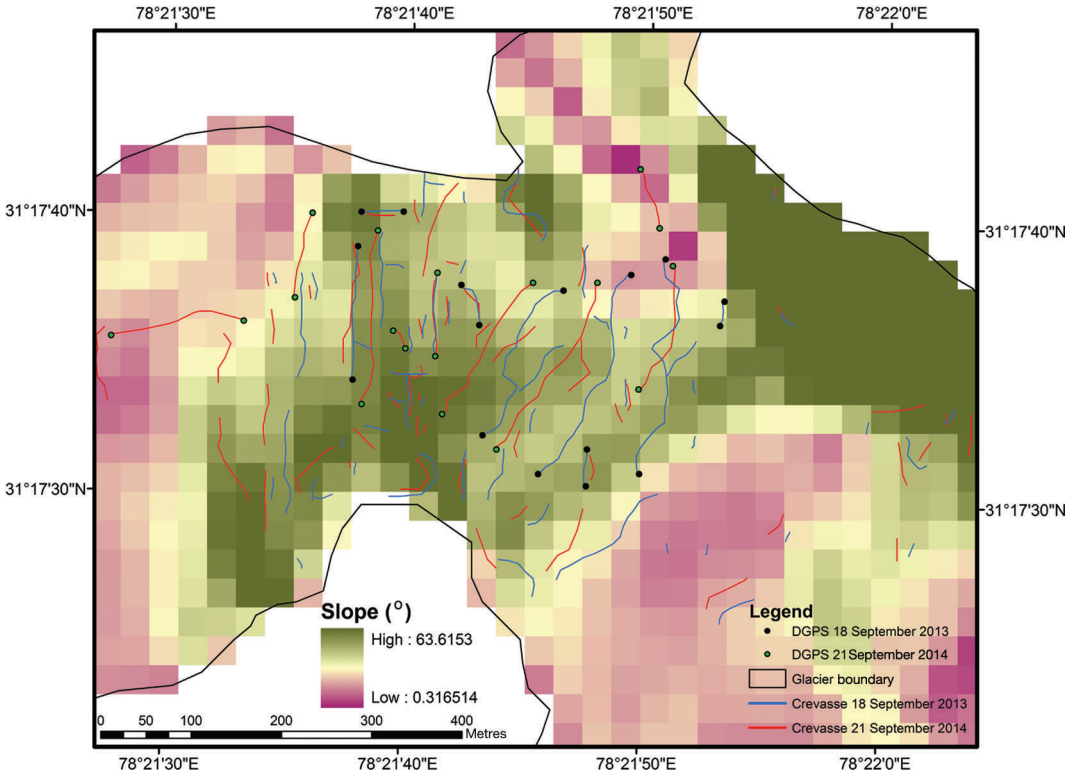

Fig. 6. DGPS observations for length comparisons of the detected crevasses. The ASTER GDEM 2-based slope pixels are in the background.

https://doi.org/10.3189/2016AoG71A496 Published online by Cambridge University Press

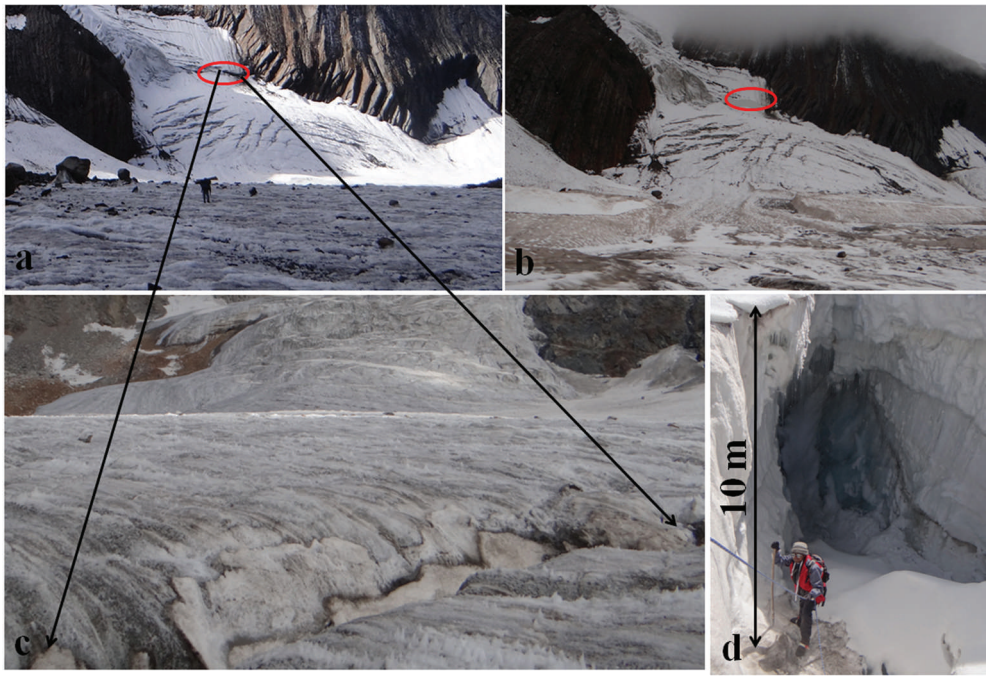

Fig. 7. The icefall and the temporally changing crevasse within red ellipse. (a) 4 August 2014; (b) 20 August 2014; (c) zoomed-in view of the reappeared crevasse on 21 September 2014; and (d) near-surface air temperature measurements 10 m inside the crevasse during the Landsat 8 pass on 18 September 2013.

Avalanching does not necessarily result in the closure of a crevasse but it can obscure the crevasse, making it undetectable in satellite imagery. The light-grey shaded portions in Figure 5 represent the mountain shadow inside the glacier area.

The algorithm was validated using DGPS field observations (Fig. 6) on the dates of two of the satellite passes (18 September 2013 and 21 September 2014). The crevasses selected for the field validation were large enough to be detected in the 15 m resolution pan-sharpened OLI multispectral bands. In all, 34 DGPS readings were taken, 16 points for 18 September 2013 and 18 points for 21 September 2014. The lengths of the crevasses were measured in situ using DGPS readings at their ends. These lengths were compared with the lengths of the automatically mapped crevasses (Fig. 8). The coefficient of determination (R^2) for the comparison of lengths of automatically mapped crevasses and DGPS-observed crevasses was very high (0.996), with a RMSE of 6.32 m and average error of 3.65%. Table 4 summarizes the average error in mapping with respect to the lengths of the crevasses. The average mapping error for larger crevasses (lengths >100 m) was higher (~6 m) than for the smaller ones (~ 3 m).

Table 4. Distribution of average error in estimates of crevasse length

Crevasse length m	Avg. error m
<50	2.98
50–100	3.25
100–150	6.98
150–200	4.11
200–250	6.77

5. DISCUSSION

The results of this study are accompanied by some interesting observations, discussed in the subsections below.

5.1. Limiting factors

Some limiting factors need to be taken into account. One prominent limiting factor was the spatial resolution of the Landsat 8 bands. Since we cannot observe or map features smaller than the spatial resolution, the 30 m multispectral resolution needed to be further improved to 15 m through pan-sharpening. The crevasses detectable by Landsat 8 on Shaune Garang glacier are present only in its accumulation zone, and the focus of discussion in the present study is only those crevasses.

Another limiting factor was seasonal snow, which covered some of the smaller fractures completely, and parts of larger fractures as well, in the images of November to

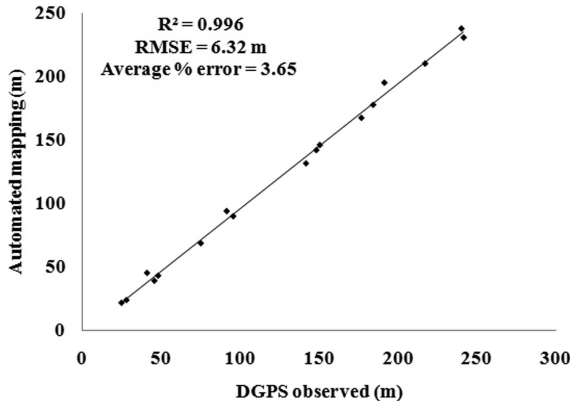

Fig. 8. Comparison of crevasse lengths measured in the field with those obtained by automated mapping.

https://doi.org/10.3189/2016AoG71A496 Published online by Cambridge University Press

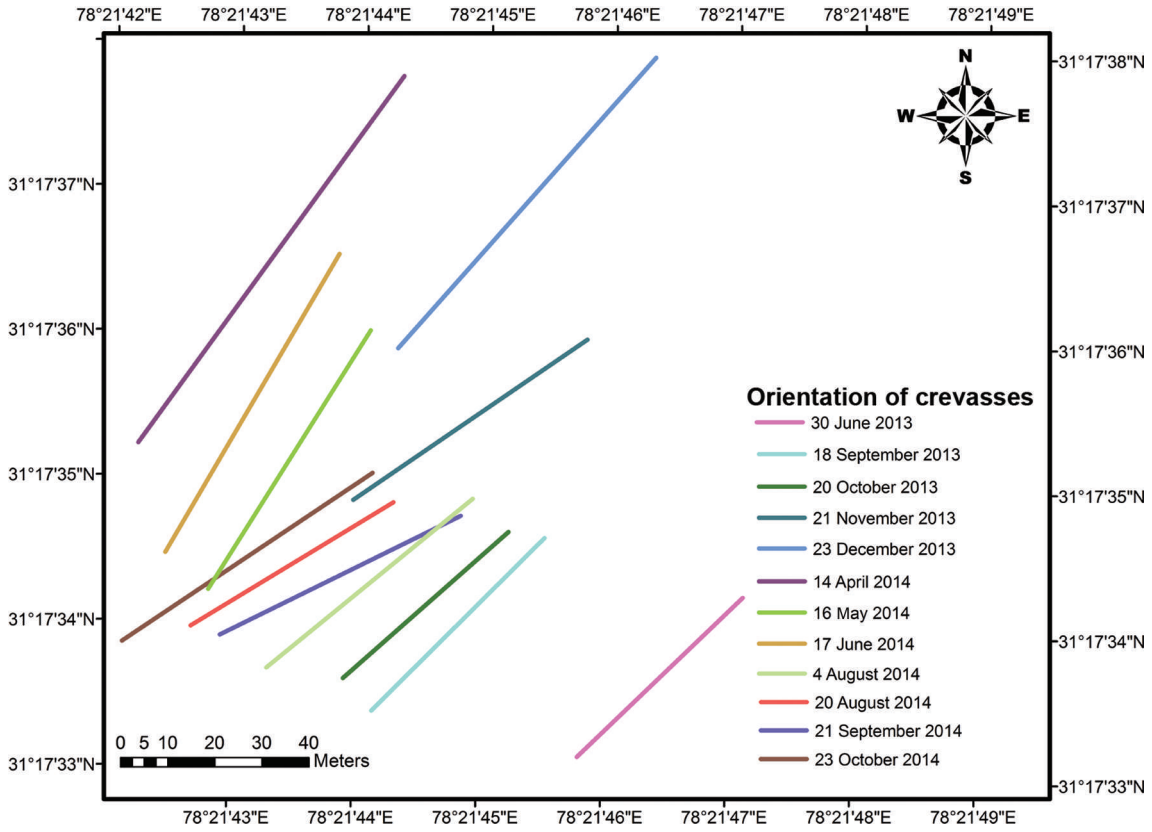

Fig. 9. Crevasse orientation on different dates, presented as mean direction and length.

April (Fig. 5). These hidden crevasses could not be detected using multispectral and thermal bands. However, their detection is possible in microwave frequencies (Eder and others, 2008). A glimpse of this was observed in the images from November to December 2013 and April to June 2014, where the number of detected crevasses was reduced considerably as compared to September's imagery.

A very important observation, particularly for Shaune Garang glacier, was the presence of seasonal mountain shadow in parts of the accumulation zone in the winter months (Fig. 5), predominantly from November to April, during Landsat 8 passes. The crevasses falling under mountain shadow could be detected using the present methodology as can be seen in the November image. In the December image, most of the crevasses were completely covered with seasonal snow.

5.2. Use of thermal band

The spectral profile analysis mentioned in Section 3.4, and by Bhardwaj and others (2015a), demonstrates a way to understand the use of at-satellite brightness temperature obtained from thermal band 10 to map the crevasses. In addition, some field-based observations were made at a few of the crevasses which were longer and wider than 15 m (Fig. 7d). During the satellite pass (10:00–11:00), sunlight reached inside these wide crevasses such that their reflections could be detected. A calibrated Kestrel Portable temperature meter (model 4300, by Nielsen-Kellerman, USA) was used to measure the change of temperature with increasing depth within the glacier. A considerable average difference of ~5 K was observed within a depth of 10 m inside the wide crevasses. Such lower temperature inside the crevasses with respect to the air temperature at the glacier surface was expected to be detectable by the TIRS (Fig. 4).

5.3. Directional mean

A spatial statistical analysis based on the method described by Mitchell (2005) was used to compute linear directional means (LDM) for the crevasses in the accumulation zone (Fig. 9) as a function of time (Fig. 6). The LDM is calculated as

$$\mathrm{LDM} = \arctan \frac{\sum_{i=1}^{n} \sin \alpha_i}{\sum_{i=1}^{n} \cos \alpha_i} \tag{3}$$

where α_i are the directions of a group of n number of mapped crevasses with respect to north. The circular variance, CV (an indication of how much the orientations deviate from the directional mean), was also calculated (Mitchell, 2005) for all the crevasses as

$$\mathrm{CV} = 1 - \frac{\sqrt{\left(\sum_{i=1}^{n} \sin \alpha_i\right)^2 + \left(\sum_{i=1}^{n} \cos \alpha_i\right)^2}}{n} \tag{4}$$

The directional statistics are summarized in Table 5.

Since the numbers of visible crevasses varied due to seasonal snow cover, especially in the winter months, only those crevasses that were present in all the images were considered for LDM calculation. Contrary to the directional mean calculation, the mean lengths given in Table 5 were calculated using all the detected crevasses and it was observed that the average of the mean lengths for November 2013 to June 2014 was 75.46 m, in contrast to 53.71 m for the rest of the observation period. This is consistent with the smaller crevasses becoming filled or covered with snow during winter.

https://doi.org/10.3189/2016AoG71A496 Published online by Cambridge University Press

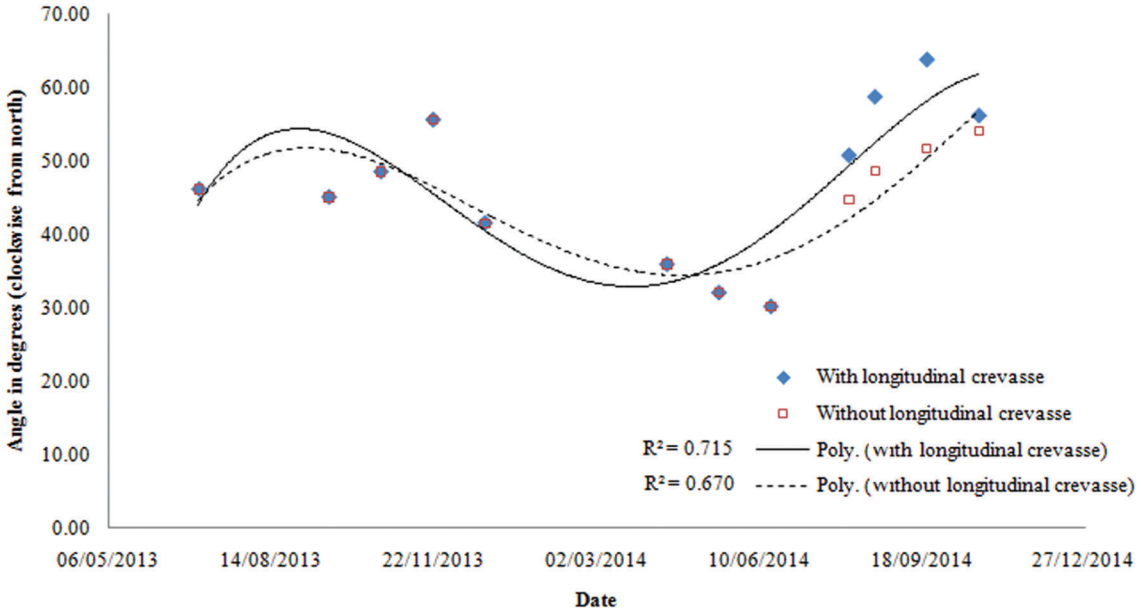

Fig. 10. Temporal variations in crevasse orientation with respect to geographical north. Date format is dd/mm/yyyy.

5.4. Annual cyclicity in the orientation of crevasses

A very interesting observation made for the temporally changing crevasse orientation was its annual cyclicity (Fig. 10). Figure 5 shows the opening of new crevasses below the icefall in the 4 August 2014 image. The most prominent of these new crevasses was a longitudinal crevasse of 150 m length. This was the only longitudinal crevasse detected in the accumulation zone of the glacier. Figure 10 shows the cyclicity in the orientations with and without the inclusion of this longitudinal crevasse.

A polynomial of fourth order was fitted to represent this cyclicity. The fit yielded coefficients of determination (R^2) of 0.72 with and 0.67 without the longitudinal crevasse The orientations were observed to be most easterly (longitudinal) during August to November and to decrease thereafter, becoming more northerly (transverse) till June. The shift from more longitudinal angles to more transverse angles can be ascribed either to closure of small longitudinal cracks or to a shift in the orientation of the larger transverse fractures. The opening of longitudinal fractures is indeed observed in Figure 5. In any case, these observations suggested an increased glacier movement during this period of the year (Dowdeswell and Collin, 1990). During the winter months, with higher accumulation load but lower temperatures, the displacements are smaller due to decreased basal sliding. Increased melting in the summer months transfers this accumulation faster towards the lower reaches of the glacier. It is also relevant in Tables 2 and 5 that the increased average orientation angle of 60° during September–October 2014, as compared to 46.8° during September–October 2013, corresponds to DGPS-based average displacement of 0.64 m, as compared to 0.39 m. Higher speed of the glacier develops larger shear stress on transverse crevasses, changing their orientations towards the direction of glacier flow, i.e. longitudinal (Hooke, 2005, p. 106–107). In the present case, the direction of glacier flow (Fig. 5) is westward. Therefore, higher glacier speed during September–October 2014 corresponded to a larger angle of 60° from north, inclined more towards the direction of glacier flow.

6. CONCLUSIONS

This study utilized Landsat 8 remotely sensed imagery in thermal and SWIR bands for developing an automated crevasse detection and mapping algorithm. The approach is original as it is based on a new band ratio for crevasse detection, wherein resampled at-satellite brightness temperature derived from thermal band 10 is divided by pan-sharpened TOA reflectance derived from SWIR band 6 to mark the crevasses. A detailed literature survey on the reflectance characteristics of crevasses, and a study of the capabilities of Landsat 8 sensors, followed by observation of the spectral profile of Landsat 8 bands along a known transect, helped in formulating this ratio. Automating the process of crevasse detection is challenging due to the presence of complex mountainous terrain, changing shadows and climatic conditions. Nonetheless, the proposed method accounts for each of these factors and provides rather high accuracy. DGPS-based observations on the days

Table 5. Statistics related to directional means of the crevasses

Date	Compass angle (clockwise from due north)	Circular variance	Mean length
dd/mm/yyyy	°		m
30/06/2013	46.21	0.41	48.85
18/09/2013	45.13	0.49	51.97
20/10/2013	48.58	0.47	46.94
21/11/2013	55.63	0.46	60.30
23/12/2013	41.61	0.31	82.55
14/04/2014	36.01	0.36	96.17
16/05/2014	32.16	0.40	64.93
17/06/2014	30.28	0.34	73.35
04/08/2014	50.78	0.57	56.66
20/08/2014	58.73	0.61	50.43
21/09/2014	63.77	0.61	57.06
23/10/2014	56.18	0.54	64.05

https://doi.org/10.3189/2016AoG71A496 Published online by Cambridge University Press

of satellite passes helped in assessing the accuracy of the outcomes. This study uses TOA reflectance and at-satellite brightness temperature derived from DN values of spectral bands of Landsat 8 sensors. The calibration constants for deriving TOA reflectance and at-satellite brightness temperature are still under investigation as Landsat 8 is a recently launched satellite. Any further modification in the calibration constants may slightly modify the threshold value without disturbing the basic logic behind the proposed ratio.

Since the crevasses on Himalayan glaciers are smaller than those on polar glaciers, their detection using moderate-resolution satellite data such as those from Landsat 8 is slightly problematic. The utilization of an appropriate pan-sharpening method increased the crevasse detection efficiency considerably in the present study. This also highlighted that continued free availability of higher spatial resolution data can help to map and study alpine glacier crevasses in a better way. From the outcomes of this study, it can be concluded that the proposed approach should be effective with any unexplored and new remote-sensing imagery in SWIR and thermal bands.

Neglecting atmospheric emission, at-satellite brightness temperature should be proportional to and indeed approximately equal to surface temperature. We had near-surface air temperature but the observations were too few to compare statistically with brightness temperatures. At this point, we can only speculate about the relationship between the two temperatures, and another study will be needed to look into this aspect. Certainly surface elevation in addition to the seasonality plays an important role in determining air temperature, and that should be another aspect of future study. However, here we would like to emphasize that in view of these uncertainties, one reason why we tried to employ the proposed band ratio throughout the year was that we were interested in the impact of seasonal variations of air temperature on the efficiency of the proposed algorithm. This is why we performed multiple DGPS observations for detected crevasses, at different temperatures and different elevations, so that we can be sure about the satisfactory functioning of the algorithm.

Another important contribution of this study is the detection of crevasses even under mountain-shadow zones. Possible explanations for such detection are hidden within the spectral profile of the at-satellite brightness temperature (Fig. 4) and field-based temperature measurements. The in situ temperature measurements suggested that even when in shadow the interiors of crevasses were sufficiently cooler than the glacier surface that they could be detected easily. This paper also discusses the presence, patterns and orientations of the crevasses with respect to the annual cyclicity in glacier movement. Once the process for automated monitoring of crevasses is developed, the next phase of this study will be focused towards developing more robust physical parameters, to measure and compare the spatially variable strains with the surface appearance of the crevasses on debris-covered Himalayan glaciers. The approach highlighted by this study requires a good understanding of the glacier studied, the data used and the logic applied before replicating it on any other glacier. The threshold for generating the final binary map of the crevasses may change, but the logic behind it and the processing steps would remain intact for a similar kind of mapping accuracy.

ACKNOWLEDGEMENTS

We are grateful to the Contribution to High Asia Runoff from Ice and Snow (CHARIS) project, funded by the United States Agency for International Development (USAID) on Shaune Garang glacier, which gave us an opportunity, while working for project objectives, to consider utilizing our field presence to verify the capabilities of Landsat 8 data for automated mapping of crevasses. We are also grateful to the chief editor, Graham Cogley, the scientific editor, Jeffrey Kargel, and two anonymous reviewers for constructive suggestions which significantly improved the quality of the paper. We thank Mritunjay K. Singh for help with DGPS data processing. We extend our gratitude to the Department of Science and Technology, Government of India, for funding our participation in the International Glaciological Society (IGS) Symposium, Kathmandu, Nepal. We further acknowledge NASA and USGS for providing Landsat 8 data free-of-cost for research purposes. Most importantly, we acknowledge the consideration and assistance provided by the IGS towards the production of this paper.

REFERENCES

Bhardwaj A and 6 others (2015a) Applicability of Landsat 8 data for characterizing glacier facies and supraglacial debris. *Int. J. Appl. Earth Obs. Geoinf.*, **38**, 51–64 (doi: 10.1016/j.jag.2014.12.011)

Bhardwaj A and 7 others (2015b) A Lake Detection Algorithm (LDA) using Landsat 8 data: a comparative approach in glacial environment. *Int. J. Appl. Earth Obs. Geoinf.*, **38**, 150–163 (doi: 10.1016/j.jag.2015.01.004)

Bindschadler RA and Scambos TA (1991) Satellite-image derived velocity field of an Antarctic ice stream. *Science*, **252**(5003), 242–246 (doi: 10.1126/science.252.5003.242)

Dowdeswell JA and Collin RL (1990) Fast-flowing outlet glaciers on Svalbard ice caps. *Geology*, **18**(8), 778–781 (doi: 10.1130/0091-7613(1990)018<0778:FFOGOS>2.3.CO;2)

Eder K, Reidler C, Mayer C and Leopold M (2008) Crevasse detection in alpine areas using ground penetrating radar as a component for a mountain guide system. *Int. Arch. Photogramm. Remote Sens. Spatial Inf. Sci.*, **37**(B8), 837–842

Hambrey MJ and Muller F (1978) Structures and ice deformation in the White Glacier, Axel Heiberg Island, Northwest Territories, Canada. *J. Glaciol.*, **20**(82), 41–66

Harper JT, Humphrey NF and Pfeffer WT (1998) Crevasse patterns and the strain-rate tensor: a high resolution comparison. *J. Glaciol.*, **44**, 68–77

Holdsworth G (1969) Primary transverse crevasses. *J. Glaciol.*, **8**, 107–129

Hooke RLeB (2005) *Principles of glacier mechanics*. Cambridge University Press, Cambridge, 106–107

Hughes T (1983) On the disintegration of ice shelves: the role of fracture. *J. Glaciol.*, **29**(101), 98–117

Joshi PK, Ghosh A, Chakraborty A, Sharma R and Joshi A (2013) Landsat again – continuing remote sensing, monitoring, mapping and measuring. *Curr. Sci.*, **105**(6), 761–763

Lever JH, Delaney AJ, Ray LE, Trautmann E, Barna LA and Burzynski AM (2013) Autonomous GPR surveys using the Polar Rover Yeti. *J. Field Robotics*, **30**(2), 194–215 (doi: 10.1002/rob.21445)

Lu D, Mausel P, Brondizio E and Moran E (2002) Assessment of atmospheric correction methods for Landsat TM data applicable to Amazon basin LBA research. *Int. J. Remote Sens.*, **23**(13), 2651–2671 (doi: 10.1080/01431160110109642)

Luckman A, Jansen D, Kulessa B, King EC, Sammonds P and Benn DI (2012) Basal crevasse in Larsen C ice shelf and implications for their global abundance. *Cryosphere*, **6**(1), 113–123 (doi: 10.5194/tc-6-113-2012)

https://doi.org/10.3189/2016AoG71A496 Published online by Cambridge University Press

Mitchell A (2005) *The ESRI guide to GIS analysis, vol. 2*. ESRI Press, Redland, CA

Naesset E (2001) Effects of differential single- and dual-frequency GPS and GLONASS observations on point accuracy under forest canopies. *Photogramm. Eng. Remote Sens.*, **67**(9), 1021–1026

Paterson WSB (1994) *The physics of glaciers*, 3rd edn. Elsevier Science, Oxford and New York, 187–190

Retzlaff R and Bentley CR (1993) Timing of stagnation of Ice Stream C, West Antarctica, from short pulse radar studies of buried surface crevasses. *J. Glaciol.*, **39**, 495–506

Rifman SS (1973) Digital rectification of ERTS multispectral imagery. *NASA Spec. Publ.* 327, 1131–1142

Shabtaie S and Bentley CR (1987) West Antarctic ice streams draining into the Ross Ice Shelf: configuration and mass balance. *J. Geophys. Res.*, **92**, 1311–1336 (doi: 10.1029/JB092iB02p01311)

Singh KK and 6 others (2013) Crevasses detection in Himalayan glaciers using ground-penetrating radar. *Curr. Sci.,* **105**(9), 1288–1295

Taurisano A, Tronstad S, Brandt O and Kohler J (2006) On the use of ground penetrating radar for detecting and reducing crevasse hazard in Dronning Maud Land, Antarctica. *Cold Reg. Sci. Technol.*, **45**, 166–177 (doi: 10.1016/j.coldregions.2006.03.005)

Van der Veen CJ (1998) Fracture mechanics approach to penetration of surface crevasses on glaciers. *Cold Reg. Sci. Technol.,* **27**, 31–47 (doi: 10.1016/S0165-232X(97)00022-0)

Vaughan DG (1993) Relating the occurrence of crevasses to surface strain rates. *J. Glaciol.,* **39**(132), 255–266

Vornberger PL and Whillans IM (1986) Surface features of Ice Stream B, Marie Byrd Land, West Antarctica. *Ann. Glaciol.*, **8**, 168–170

Vornberger PL and Whillans IM (1990) Crevasse deformation and examples from Ice Stream B, Antarctica. *J. Glaciol.*, **36**, 3–9

Whillans, IM and Tseng YH (1995) Automatic tracking of crevasses on satellite images. *Cold Reg. Sci. Technol.*, **23**, 201–214 (doi: 10.1016/0165-232X(94)00009-M)

Whillans IM, Jackson M and Tseng YH (1993) Velocity pattern in a transect across Ice Stream B, Antarctica. *J. Glaciol.*, **39**, 562–572

Zamora R and 7 others (2007) Crevasse detection in glaciers of southern Chile and Antarctica by means of ground penetrating radar. *IAHS Publ.* 318 (Assembly in Foz do Iguaçu 2005 – *Glacier Mass Balance Change and Meltwater Discharge*)

Zhang Y (2004) Understanding image fusion. *Photogramm. Eng. Remote Sens.,* **70**(6), 657–661

Zhou C, Dongchen E, Wang Z and Sun J (2008) Remote sensing application in Antarctic inland areas. *Int. Arch. Photogramm. Remote Sens. Spatial Inf. Sci.*, **37**(B8), 819–824

https://doi.org/10.3189/2016AoG71A496 Published online by Cambridge University Press